RSC Advances

PAPER

View Article Online
View Journal | View Issue

Cite this: *RSC Adv.*, 2024, **14**, 8445

Hetastarch-stabilized polypyrrole with hyperthermia-enhanced release and catalytic activity for synergistic antitumor therapy

Xiaoyun Huang,†[ac] Zhiming Liu,†[b] Weijian Zeng,†[d] Xiaoyu Ma,[a] Yu Zhang,[c] Muye Li,[c] Jiutong Sun,[d] Sheng Mao*[a] and Li Bian*[c]

Fenton catalytic medicine that catalyzes the production of ·OH without external energy input or oxygen as a substrate has reshaped the landscape of conventional cancer therapy in recent decades, yet potential biosafety concerns caused by non-safety-approved components restrict their clinical translation from the bench to the bedside. Herein, to overcome this dilemma, we elaborately utilizate safety-approved hetastarch, which has been extensively employed in the clinic as a plasma substitute, as a stabilizer participating in the copper chloride-initiated polymerization of pyrrole monomer before loading it with DOX. The constructed DOX-loaded hetastarch-doped Cu-based polypyrrole (HES@CuP-D) catalyzes the excess H_2O_2 in tumor cells to ·OH through a Cu^+-mediated Fenton-like reaction, which not only causes oxidative damage to tumor cells but also leads to the structural collapse and DOX release. Additionally, HES@CuP-D together with laser irradiation reinforces tumor killing efficiency by hyperthermia-enhanced catalytic activity and -accelerated drug release. As a result, the developed HES@CuP-D provides a promising strategy for Fenton catalytic therapy with negligible toxicity to the body.

Received 4th December 2023
Accepted 26th February 2024

DOI: 10.1039/d3ra08263f

rsc.li/rsc-advances

1. Introduction

Chemodynamic therapy, which catalyzes hydrogen peroxide (H_2O_2) into highly toxic hydroxyl radicals (·OH) *via* Fenton or Fenton-like reactions to trigger tumor cell death, has attracted increasing attention in recent decades.[1–3] The utilization of Fenton agents and endogenous H_2O_2 to generate ·OH eliminates the requirement for external energy input or oxygen as a substrate, effectively avoiding the primary obstacles of tumor hypoxia-associated resistance and restricted light penetration depth encountered in cancer photodynamic therapy.[4–9] As is well known, considerable efforts have been devoted to developing versatile Fenton nanomedicines, including Cu^+-based ones with a high reaction rate (1×10^4 m^{-1} s^{-1}) that initiate rapid and robust ·OH production under both weakly acidic and neutral conditions.[10–13] Although these Cu^+-based Fenton nanomedicines have demonstrated promise antitumor effects, less emphasis has been made on their biodegradability and biosafety, especially in terms of potential long-term toxicity caused by non-safe components. Potential biosafety issues, for instance, include but are not limited to the introduction of organic chemicals (such as commonly used polyvinyl alcohol, polyvinylpyrrolidone, or chloroform) during manufacturing processes, as well as hazardous metabolic byproducts within the body.[14,15] As far as this is concerned, the application of safety-approved components in manufacturing Cu^+-based Fenton nanomedicines is highly desirable for achieving a satisfactory anticancer effect with minimal toxicity.

As an important conjugated polymer, polypyrrole (PPy) is characterized by a large π-electronic delocalized backbone and inter-doping with oxidant complexes and stabilizers, which confers potent photothermal and photo-electronic advantages.[16–19] These features have been widely utilized in biological applications, such as photothermal therapy (PTT), drug delivery, tissue engineering, and biosensors.[20–22] For instance, various PPy morphologies have been developed for near infrared (NIR) laser-mediated PTT against malignant tumors, including ultrasmall PPy smaller than 10 nm, two-dimensional PPy, hollow PPy, and so on.[23–25] In addition to being utilized as a photothermal agent, PPy doped with various metal ions (such as Fe^{2+}, Cu^+, and Mn^{2+}) is also equipped with the Fenton therapy capability, which can be enhanced further by PTT-induced hyperthermia, as previously reported.[26–29] Up to now, the pharmacologically active component of metal oxidants has been flourishingly focused and optimized, nevertheless, another key component of stabilizers that pass through the bulk to the surface has gone unnoticed, despite being critical for

[a]*School of Clinical Medicine, Qujing Medical College, Qujing, 655100, Yunnan, China. E-mail: hhuo0010@163.com*

[b]*Department of Urinary, Qujing No. 1 Hospital, Qujing, 655000, Yunnan, China*

[c]*Department of Pathology, The First Affiliated Hospital of Kunming Medical University, Kunming, 650032, Yunnan, China. E-mail: bianli1976@sina.com*

[d]*College of Science and Technology, Ningbo University, Ningbo, 315300, Zhejiang, China*

† These authors contributed equally to this work.

structural biosafety and degrading characteristics.[30–32] Polyvinylpyrrolidone and polyvinyl alcohol, two popular stabilizers, are susceptible to delayed degradation and prolonged metabolic clearance *in vivo*, posing a potential risk of long-term toxicity and future hurdles to clinical translation. As a result, developing biodegradable and biosafe PPy, particularly those consisting of safety-approved pharmaceutic adjuvants, is crucial for their biological applications.

Hetastarch (HES) is a semi-synthetic polysaccharide that has been extensively employed in the clinic as a plasma substitute due to its excellent immunocompatibility and low allergy rate.[33–36] It is interesting that HES has analogous structure and physicochemical characteristics with polyvinyl alcohol, such as abundance hydroxyl groups, good water solubility, and solvent stability.[37,38] Inspired by this, we innovatively developed a one-step synthesis approach for HES-doped Cu-based PPy (termed as HES@CuP) by using copper chloride as an oxidant and replacing traditional polyvinyl alcohol with HES as a stabilizer (Scheme 1). Polyvalent Cu ions-doped HES@CuP exhibited excellent dispersity, good biocompatibility, and hyperthermia-enhanced Fenton catalytic activity, triggering oxidative damage to tumor cells without affecting normal cellular activity. After doxorubicin (DOX) loading, the resulting HES@CuP-D showed hyperthermia-accelerated release and degradation behavior in a tumor simulation microenvironment. By the synergistic killing effect of DOX and HES@CuP, the significant tumor cell death could be achieved. Overall, this work not only presented a novel PPy based on safety-approved HES with hyperthermia-accelerated release and degradation but also promoted the development of Fenton catalytic therapy.

2. Experimental section

2.1. Materials and chemicals

Pyrrole (99%), methylene blue (MB), and copper chloride ($CuCl_2$) were purchased from Aladdin. Hetastarch (HES) and doxorubicin hydrochloride (DOX) were obtained from Shanghai Yuanye Bio-Technology Co., Ltd. 2-(4-Amidinophenyl)-6-indolecarbamidine dihydrochloride (DAPI) was purchased from Solarbio. 2′,7′-Dichlorofluorescin diacetateb (DCFH-DA), 3-(4,5-dimethylthiazol-2-yl)-2,5-dipheny-ltetrazolium bromide (MTT), and JC-1 probe were obtained from Beyotime Biotechnology. Dulbecco's modified eagle's medium (DMEM), phosphate buffer (PBS), fetal bovine serum, and trypsin–EDTA were obtained from Gibco-BRL. All chemicals and reagents were of the highest quality commercially available and used without further purification.

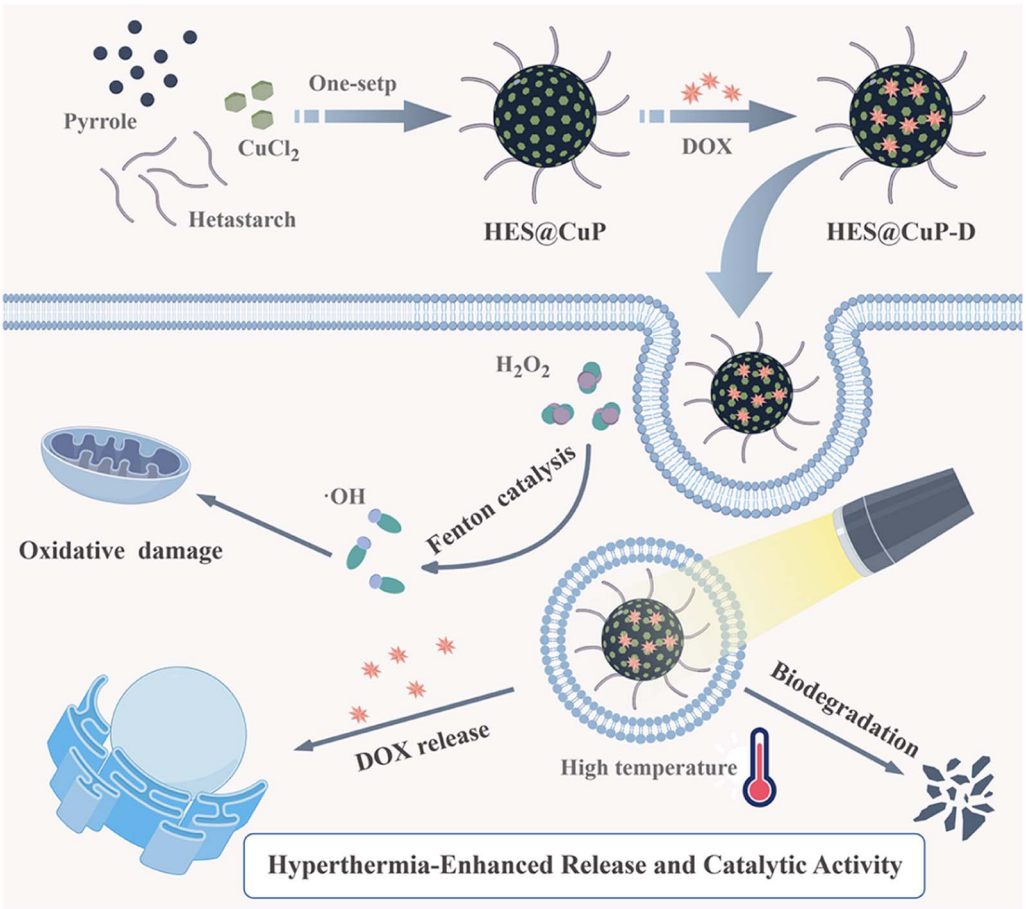

Scheme 1 The schematic illustration of the synthetic procedure of HES@CuP-D and its synergistic antitumor therapy.

2.2. Synthesis of HES@CuP

In a 100 round-bottom flask, 500 mg HES and 10 mL deionized (Di) water were added and gently stirred for 1 h at room temperature. Then, 750 mg of $CuCl_2$ pre-dissolved in 10 mL Di water was slowly added and continuously stirred for 30 min. Subsequently, 200 μL of pyrrole monomer was added to the above mixture and stirred for 20 h. The mixture was centrifuged at 18 000 rpm for 15 min to collect the precipitate, which was washed three times with Di water.

2.3. Synthesis of HES@CuP-D

10 mg of DOX were added to 10 mL of HES@CuP (10 mg, dispersed in PBS) under magnetic stirring at room temperature. 24 h later, the mixture was purified in a dialysis bag (3000 D) for 24 h. The obtained HES@CuP-D nanoparticles were stored at 4 °C for further experiments.

2.4. Characterization

To characterize the microstructure and morphology of nanoparticles, transmission electron microscopy (TEM) was performed on a JEM-2100UHR microscope (JEOL, Japan). X-ray photoelectron spectroscopy (XPS, ESCALAB 250Xi, Japan), X-ray diffraction (XRD, Bruker D8, Germany), and Fourier transform infrared spectrophotometer spectrum (FTIR, Nicolet6700-Contiuμm, Thermo, USA) were carried out to analyze the chemical compositions and crystal structures of HES@CuP. UV-vis-NIR spectrum of HES@CuP and HES@CuP-D was investigated by using an Infinite M200 PRO spectrophotometer. The zeta potential and corresponding hydrodynamic particle size of HES@CuP and HES@CuP-D were detected through dynamic light scattering (DLS, 90Plus PALS, Brookhaven, UK). The scheme illustration was drawn by Figdraw.

2.5. Photothermal conversion performance

An IR thermal camera (Ti480U, Fluke, USA) was used to monitor the temperature changes with exposure duration to assess the photothermal conversion performance of HES@CuP-D. In particular, various concentrations of HES@CuP or HES@CuP-D solutions (0, 100, 200, and 300 μg/mL) were subjected for 10 min to an 808 nm laser at various power densities (0.59, 0.99, 1.38, and 2.00 W/cm^2), while pure water served as a control. In addition, to assess the photothermal stability, HES@CuP-D (200 μg/mL) was irradiated by the 808 nm laser (1.38 W/cm^2) for five switching cycles (on/off: 6 min/6 min).

2.6. *In vitro* ·OH generation

The ·OH generation capability of HES@CuP-D was assayed by MB probe. Briefly, 7 μg/mL of MB and different amount of H_2O_2 (0, 1, and 5 mM) were added to HES@CuP-D solutions. In the presence or absence of 808 nm laser irradiation, the absorbance of diverse mixtures was measured by UV-vis-NIR spectrometer.

To further identify the generation of ·OH, a certain quantity of HES@CuP-D was mixed with H_2O_2 (5 mM) and 5,5-dimethyl-1-pyrrolineN-oxide (DMPO) in the absence or presence of laser irradiation. Subsequently, the ·OH signal was detected and recorded using Electron Spin Resonance (ESR).

2.7. Hyperthermia-accelerated DOX release and degradation

In vitro DOX release experiments were performed by dialysis in PBS at different H_2O_2 concentrations and the results were detected using a UV-vis-NIR spectrometer. Briefly, 1 mL of HES@CuP-D (1 mg/mL) nanoparticles were dialyzed with PBS (9 mL) containing different H_2O_2 concentrations (0, 1, and 5 mM) at 37 °C while continuously shaking in the dark. For the laser requirement groups, an 808 nm laser (1.38 W/cm^2 for 10 min) was used to irradiate the mixture at 4 and 8 h. At the specified time points (0.33, 0.66, 1, 2, 4, 6, 8, 19, 23, 27, 30, 43, and 48 h), the amount of released DOX was measured using UV-vis-NIR spectrometer. Finally, the degradation behavior of HES@CuP-D was evaluated by TEM.

2.8. Cellular experiments

Mouse fibroblast cells (3T3) and human pulmonary adenocarcinoma cells (A549) were purchased from the American Type Culture Collection and cultured in DMEM cell culture medium at 37 °C under 5% CO_2.

2.9. Cell cytotoxicity

The cytotoxicity of HES@CuP on cells was assessed by the standard 3-(4,5-dimethylthiazol-2-yl)-2,5-dipheny-ltetrazolium bromide (MTT) assay. Briefly, cancer cells A549 or normal cells 3T3 were inoculated into 96-well plates at a density of 8000 cells per well and co-cultured at 37 °C for 24 h. Subsequently, the medium was replaced with fresh medium containing different concentrations of HES@CuP (0, 12.5, 25, 50, 100, 200, and 400 μg/mL). After 24 h of co-incubation, cells were washed twice with PBS and analyzed using the standard protocol of MTT assay.

To further evaluate the *in vitro* photothermal cytotoxicity of HES@CuP-D, A549 cells were treated with PBS, DOX, HES@CuP, or HES@CuP-D (equal HES@CuP concentration: 200 μg/mL) for 12 h. Afterward, cells in the laser-required groups were exposed to an 808 nm laser with a power density of 1.38 W/cm^2 for 6 min and continued to be incubated for 24 h. Finally, the cells were washed twice with PBS and cell viability was measured according to the standard protocol of MTT assay.

2.10. Intracellular ·OH generation

A549 cells (2×10^5 cells per dish per well) were seeded in confocal dishes and incubated for 24 h. Then PBS, HES@CuP, or HES@CuP-D was added to the cells and co-incubated for 12 h. Cells in laser-treated groups were irradiated with 808 nm laser (1.38 W/cm^2) for 6 min. All cells were replaced with DMEM containing 2′,7′-dichlorofluorescin diacetateb (DCFH-DA, 10 μM) and incubated for 30 min. Then, cells were washed three times with PBS, and analyzed using flow cytometer and visualized by Confocal Laser Scanning Microscope (CLSM, FV3000, Olympus, Japan).

2.11. Mitochondrial membrane potential

Mitochondrial membrane potential assay was conducted by JC-1 probe. A549 cells were seeded in confocal dish (2×10^5 cells per dish) and incubated overnight. Then, the cells were treated with PBS, HES@CuP, or HES@CuP-D for 12 h. After that, the cells in laser groups were exposed to 808 nm laser irradiation (1.38 W/cm^2) for 6 min. The cells were stained with JC-1 dye for 15 min, and the images were acquired by CLSM.

2.12. Statistical analysis

All statistical analyses were used GraphPad Prism. The results of statistical analysis were presented as mean ± SD. Statistical significance was calculated by one-way ANOVA analysis. The statistical significance was defined as $*p < 0.05$; $**p < 0.01$; $***p < 0.001$.

3. Results and discussion

HES@CuP, a novel Fenton nanomedicine, was prepared *via* one-step oxidation polymerization using pharmacodynamic component $CuCl_2$ as the oxidant, safety-approved HES as the stabilizer, and pyrrole as the polymer monomer. The transmission electron microscopy (TEM) images at low magnification revealed that the obtained HES@CuP had a spherical morphology with uniform size and good dispersion (Fig. 1A). Its hydrodynamic particle size and polydispersity index were next measured to be 102 nm and 0.089, respectively, using the dynamic light scattering technique (Fig. 1B). To further identify the structural features and chemical composition of HES@CuP, X-ray diffraction (XRD) spectroscopy, X-ray photoelectron spectroscopy (XPS), and Fourier transform infrared (FTIR) spectra were carried out. The amorphous nature and intermolecular stacking structure of HES@CuP were demonstrated by the broad characteristic peak in Fig. 1C from 14 to 30°. In terms of XPS detection, C, N, O, and Cu elements were all observed in HES@CuP, initially confirming that the PPy structure (representing C and N elements), the co-doping of HES (representing O element) and Cu ions (representing Cu element) have been successfully fabricated (Fig. 1D). More importantly, the high-resolution XPS spectra of Cu 2p revealed its monovalent and divalent Cu states, with two peaks at 932.55 eV and 934.48 eV associated with the Cu $2p_{3/2}$ of Cu^+ and Cu^{2+}, respectively, and the other peaks at 952.20 eV and 954.30 eV corresponded to the Cu $2p_{1/2}$ of Cu^+ and Cu^{2+}, respectively (Fig. 1E). The ratio of Cu^+ to Cu^{2+} in prepared HES@CuP was determined to be 2.6 : 1. In addition, the characteristic peaks appearing at 1521, 1423, 1289, and 1148 cm^{-1} in the FTIR spectra of HES@CuP belonged to the C=C, C–N, C–H, and C–C stretching vibrations in the typical PPy framework, respectively, which indicated the presence of the intact chemical structure of PPy in HES@CuP (Fig. 1F). Meanwhile, the absorption peak at 1008 cm^{-1} was assigned to the stretching vibration of C–O in the HES structure, further demonstrating the successful doping of HES during the polymerization process.

The most commonly administered broad-spectrum antitumor drugs, DOX, was then coupled to HES@CuP by π–π stacking and electrostatic interaction, ultimately yielding HES@CuP-D. The TEM images in Fig. 2A revealed that DOX

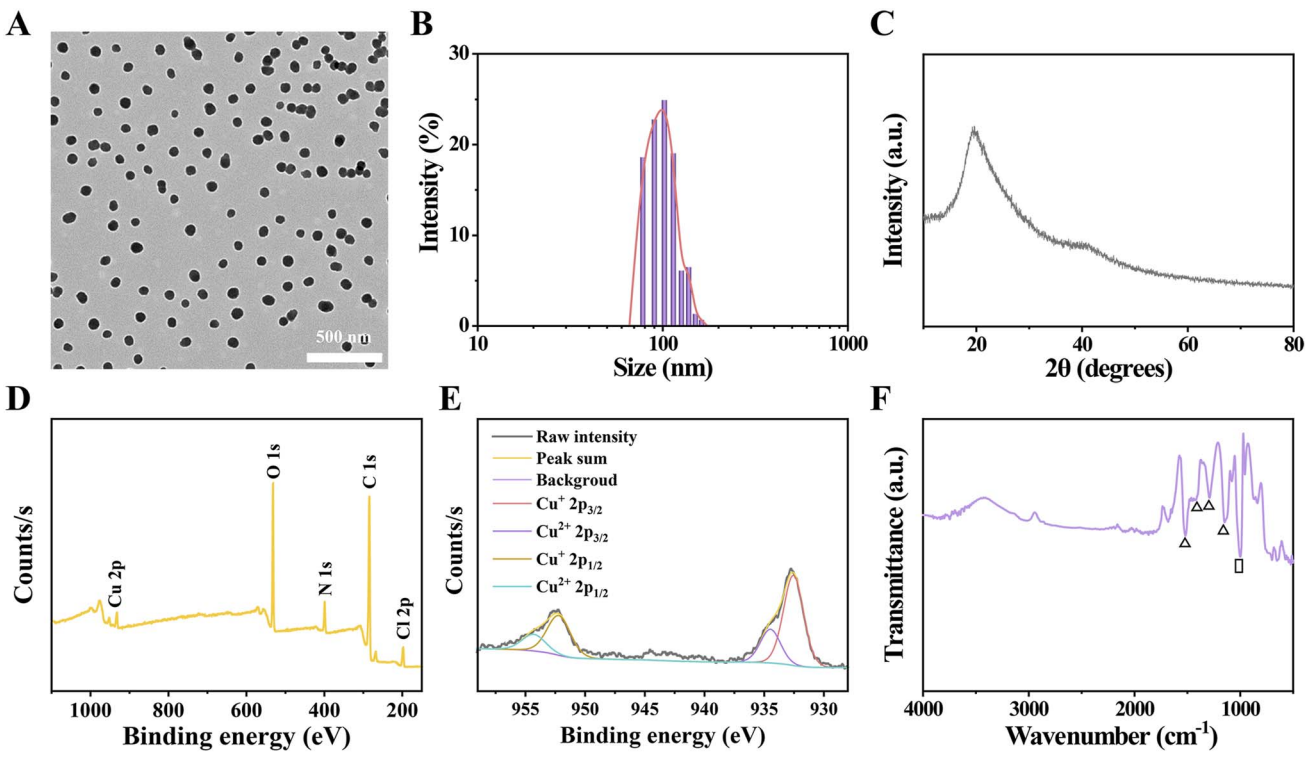

Fig. 1 (A) TEM image and (B) hydrodynamic particle size of HES@CuP. (C) XRD, (D) full XPS, (E) high-resolution Cu 2p XPS, and (F) FTIR spectra of HES@CuP. The triangles and rectangles represented the characteristic absorption peaks of PPy and HES, respectively.

loading had no discernible impact on the morphology or TEM size of nanoparticles, while the surface zeta potential of HES@CuP-D increased from −38.35 eV to 27.78 eV (Fig. 2B). The optical properties of HES@CuP and HES@CuP-D were evaluated using UV-vis-NIR spectrometry. As shown in Fig. 2C, HES@CuP revealed a strong and broad absorbance from vis to NIR. Following DOX loading, a distinctive DOX absorption peak at 480 nm was found in HES@CuP-D, with concentration-dependent increase of absorption singal (Fig. 2D and E). The loading capacity of DOX was calculated to be 22.2%. Furthermore, HES@CuP-D demonstrated good stability and dispersibility over a period of 7 days in a variety of physiological media, including pure H_2O, PBS, and DMEM (Fig. 2F).

To investigate the photothermal property, Fenton catalytic activity, hyperthermia-accelerated release and degradability of HES@CuP-D, the corresponding temperature monitoring, ·OH generation, and TEM images were performed. Initially, the photothermal conversion efficiency was assessed by monitoring the real-time temperature variations of HES@CuP or HES@CuP-D under 808 nm laser irradiation, with pure H_2O as a control. As revealed in Fig. 3A and B, the temperature of HES@CuP and HES@CuP-D increased rapidly with the elevated concentrations and extended irradiation time, rising to 57.77 and 55.60 °C within 10 min at a concentration of 200 μg/mL, respectively. Under tha same settings, however, pure H_2O showed a negligible temperature change. Moreover, a laser power-dependent temperature increase of HES@CuP-D was also observed in Fig. 3C. Within five switching cycles of 808 nm laser irradiation, HES@CuP-D displayed similar heating and cooling temperature profiles, demonstrating its excellent photostability (Fig. 3D). According to the single photothermal heating and cooling curve in Fig. 3E, the thermal time constant (τ_s) and photothermal conversion efficiency (η) of HES@CuP-D was calculated to be 126.74 and 19.15%, respectively. All of the preceding findings suggested that HES@CuP-D was a powerful photothermal agent capable of causing PTT on malignancies.

After that, the Fenton catalytic activity of HES@CuP-D with or without 808 nm laser irradiation was investigated at different H_2O_2 concentrations using the methylene blue (MB) indicator. Fig. 3F revealed that increasing the H_2O_2 concentration resulted in increased MB degradation, suggesting the production of ·OH and satisfactory Fenton catalytic activity of HES@CuP-D. In contrast, following laser exposure, the degradation of MB was further increased at the same H_2O_2 concentration (5 mM), indicating that the induced hyperthermia effect could boost the Fenton catalytic process. The electron spin resonance (ESR) measurements presented the similar outcomes with MB degradation experiments, further confirming the hyperthermia-enhanced Fenton reaction and ·OH generation (Fig. 3G). The DOX released from HES@CuP-D was then analyzed in PBS solution under various H_2O_2 conditions. As shown in Fig. 3H, the quantity of DOX released after 48 h incubation was only 15.94% in the absence of H_2O_2, but rose to 34.26% and 59.61% in the presence of 1 mM H_2O_2 and 5 mM H_2O_2, respectively, suggesting the H_2O_2 concentration-dependent release behavior of DOX. Impressively, the simultaneous stimulation of an 808 nm laser and 5 mM H_2O_2 dramatically boosted DOX release to 71.57% in equal incubation time, which was attributed to

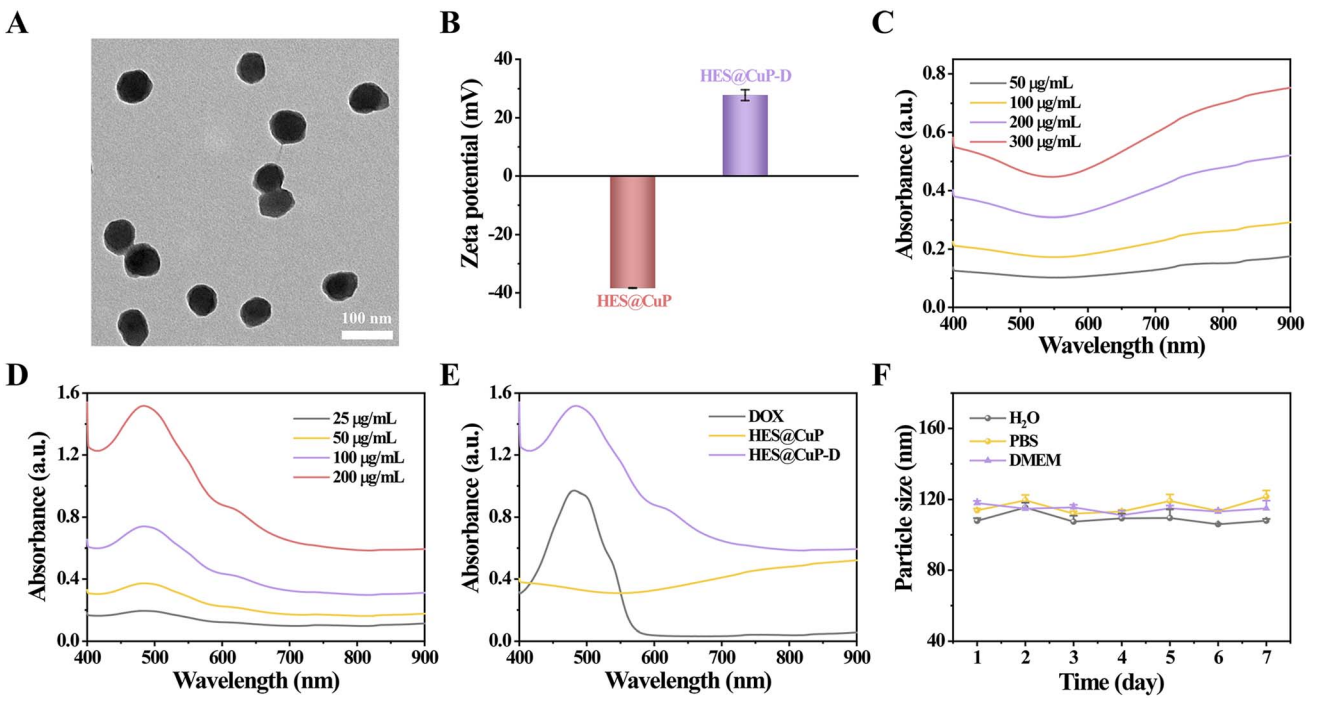

Fig. 2 (A) TEM image of HES@CuP-D. (B) Zeta potentials of HES@CuP and HES@CuP-D. Vis-NIR absorbance spectra of (C) HES@CuP or (D) HES@CuP-D at varied concentrations. (E) Vis-NIR absorbance spectra of free DOX, HES@CuP, and HES@CuP-D. (F) Colloidal stability of HES@CuP-D in H_2O, PBS, and DMEM for 7 days.

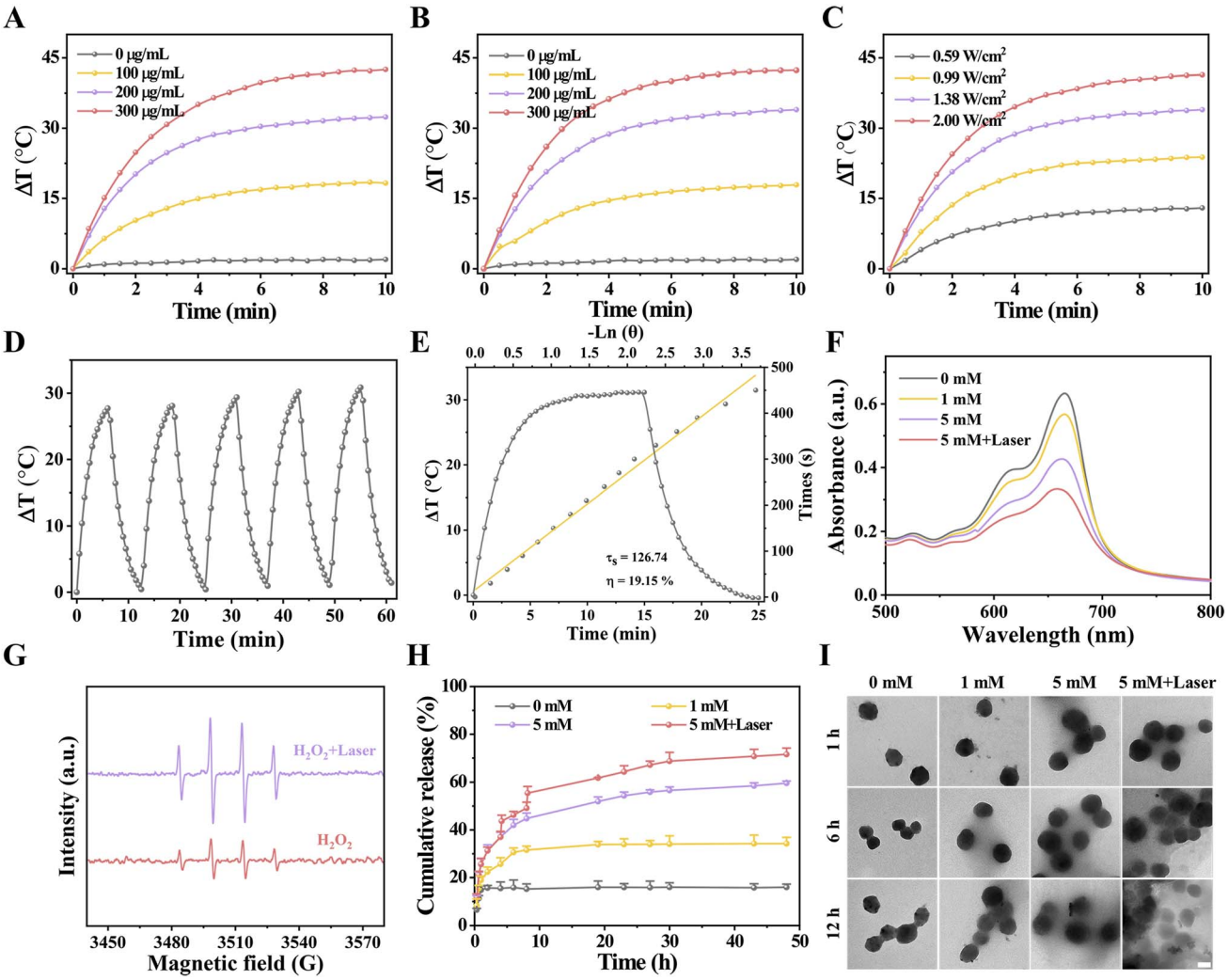

Fig. 3 Temperature change curves of (A) HES@CuP or (B) HES@CuP-D at various concentrations (0, 100, 200, and 300 μg/mL) under 808 nm laser (1.38 W/cm^2) irradiation for 10 min. (C) Temperature change curves of HES@CuP-D under 808 nm laser irradiation at varied power densities (0.59, 0.99, 1.38, and 2.00 W/cm^2) for 10 min. (D) Photothermal conversion stability of HES@CuP-D solution under irradiation with five on/off cycles. (E) Photothermal heating and cooling curves of HES@CuP-D under 808 nm laser irradiation, and corresponding linear relationship between time and −ln θ from the cooling period. (F) The degradation of MB caused by HES@CuP-D at different H_2O_2 concentrations (0, 1, and 5 mM) with or without laser irradiation. (G) ESR spectra of ·OH generated by HES@CuP-D under varied reaction conditions. (H) DOX release profiles and corresponding (I) TEM images of HES@CuP-D treated with different concentrations of H_2O_2 with or without laser irradiation, scale bar: 50 nm.

hyperthermia-accelerated release. Meanwhile, TEM characterization was also used to investigate the hyperthermia-accelerated degradability of HES@CuP-D. After 12 h of incubation without H_2O_2, the structure and morphology of HES@CuP-D remained relatively intact while the structural collapse and dissolution of HES@CuP-D gradually deteriorated after 12 h of incubation in 1 mM H_2O_2 and 5 mM H_2O_2 (Fig. 3I). Consistent with the DOX release experiment, 5 mM H_2O_2 plus laser induced the strongest biodegradation.

The anticancer effects of HES@CuP-D were then investigated at the cellular level due to its good photothermal property and Fenton catalytic activity, as well as hyperthermia-accelerated release and degradability. First, the cytotoxicity of HES@CuP against normal cells (3T3 cells) and cancer cells (A549 cells) was examined using MTT assay. As seen in Fig. 4A, HES@CuP exhibited negligible cytotoxicity on 3T3 cells even at a relatively high concentration of 400 μg/mL. Conversely, HES@CuP caused concentration-dependent cell death in A549 cells, which might be due to the presence of a mature antioxidant system in normal cells but overexpressed H_2O_2 in tumor cells. It is noteworthy that the viability of A549 tumor cells further decreased following treatment with HES@CuP-D and reached a nadir when treated with HES@CuP-D+L, which well confirmed the hyperthermia-enhanced Fenton catalytic activity and synergistic antitumor effect (Fig. 4B). Moreover, the synergistic strategy of chemotherapy and Fenton therapy was more effective than the effectiveness of any single therapy.

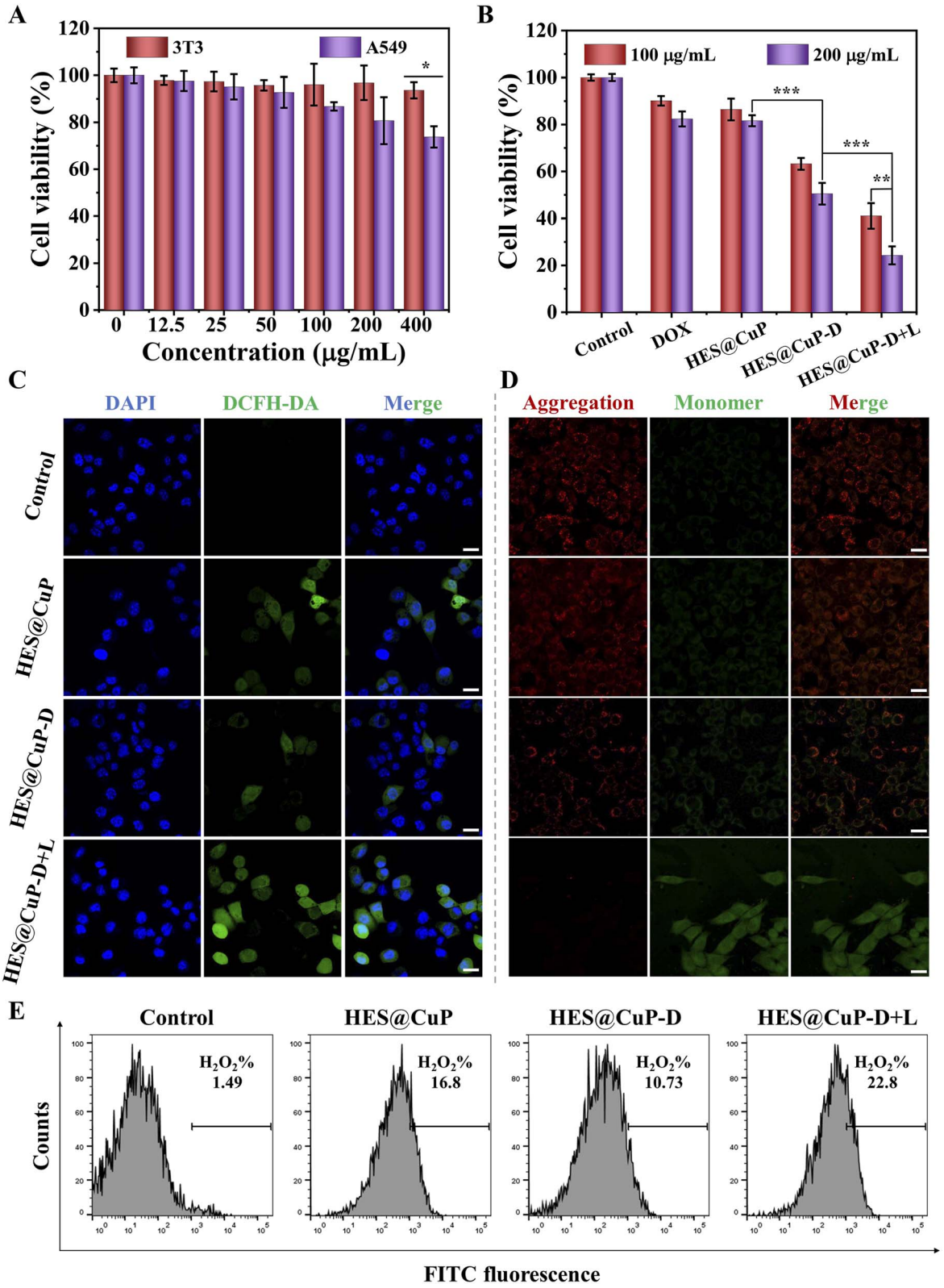

Fig. 4 (A) Relative cell viabilities of 3T3 and A549 cells after treatment with different concentrations of HES@CuP. (B) Relative cell viabilities of A549 cells after receiving different treatments. (C) CLSM images of intracellular ·OH level in A549 cells after receiving different treatments, scale bar: 20 μm. (D) CLSM images of mitochondrial membrane potential in A549 cells after different treatments, scale bar: 20 μm. (E) Flow cytometry of intracellular ·OH level in A549 cells after receiving different treatments. Statistical significance was calculated by one-way ANOVA analysis. *P < 0.05, **P < 0.01, ***P < 0.001.

To explore the therapeutic mechanism of HES@CuP-D, 2′,7′-dichlorodihydrofluorescein diacetate (DCFH-DA) and mitochondrial membrane potential detection probe (JC-1) were adopted to assess the intracellular ·OH generation and mitochondrial function. As shown in Fig. 4C, A549 cells treated with HES@CuP or HES@CuP-D alone showed a modest ·OH generation in comparison to the control group, which was attributed to the Fenton-like effect. However, HES@CuP-D with 808 nm laser irradiation resulted in the highest intracellular ·OH generation, reconfirming hyperthermia-enhanced Fenton catalytic activity, which was responsible for the potent tumor killing. This phenomenon was reconfirmed by corresponding flow cytometry results in Fig. 4E. Consistent with the intracellular ·OH change, the red-to-green fluorescence intensity ratio dramatically dropped and red fluorescence was hardly visible, suggesting severe mitochondrial damage (Fig. 4D).

4. Conclusions

In this work, we have presented a biocompatible and biodegradable HES@CuP by one-step synthesis method using safety-approved HES as a novel stabilizer and $CuCl_2$ as an oxidant, which was whereafter utilized to be a carrier encapsulating DOX for hyperthermia-accelerated drug release and Fenton catalytic damage to lung cancer cells. Because of the doping of polyvalent Cu ions, the resulting HES@CuP-D catalyzed the generation of ·OH from overexpressed H_2O_2 in tumor cells, which leaded to oxidative damage and even tumor cell death, while exhibiting insignificant toxicity to normal cells. Concomitantly, its nanomorphology and chemical structure disintegrated, allowing cargo DOX to be released and exert antitumor effect. More importantly, those processes are further facilitated by the laser-induced hyperthermia effect, ultimately resulting in severe oxidative damage and tumor cell death. Collectedly, the HES@CuP-D developed here not only provides an efficient approach for preparing hetastarch-stabilized PPy but also opens up a new avenue for the clinical design of prospective nanomedicines with safety-approved compositions.

Conflicts of interest

There are no conflicts to declare.

Acknowledgements

This study was supported by the Yunnan Provincial Science and Technology Department-Applied Basic Research Joint Special Funds of Chinese Medicine 2019FF002(-057) and Yunnan Fundamental Research Projects 202201AY070001-213.

References

1 Z. Tang, P. Zhao, H. Wang, Y. Liu and W. Bu, Biomedicine meets Fenton chemistry, *Chem. Rev.*, 2021, **121**(4), 1981–2019.
2 H. Hu, W. Feng, X. Qian, L. Yu, Y. Chen and Y. Li, Emerging nanomedicine-enabled/enhanced nanodynamic therapies beyond traditional photodynamics, *Adv. Mater.*, 2021, **33**(12), 2005062.
3 W. Zeng, H. Zhang, X. Yuan, T. Chen, Z. Pei and X. Ji, Two-dimensional nanomaterial-based catalytic medicine: theories, advanced catalyst and system design, *Adv. Drug Delivery Rev.*, 2022, **184**, 114241.
4 Z. Tang, Y. Liu, M. He and W. Bu, Chemodynamic therapy: tumour microenvironment-mediated Fenton and Fenton-like reactions, *Angew. Chem., Int. Ed.*, 2019, **58**(4), 946–956.
5 H. Lin, Y. Chen and J. Shi, Nanoparticle-triggered *in situ* catalytic chemical reactions for tumour-specific therapy, *Chem. Soc. Rev.*, 2018, **47**(6), 1938–1958.
6 Y. Yang, W. Zeng, P. Huang, X. Zeng and L. Mei, Smart materials for drug delivery and cancer therapy, *View*, 2021, **2**(2), 20200042.
7 Y. Nie, W. Zhang, W. Xiao, W. Zeng, T. Chen, W. Huang, X. Wu, Y. Kang, J. Dong, W. Luo and X. Ji, Novel biodegradable two-dimensional vanadene augmented photoelectro-Fenton process for cancer catalytic therapy, *Biomaterials*, 2022, **289**, 121791.
8 W. Zeng, H. Zhang, Y. Deng, A. Jiang, X. Bao, M. Guo, Z. Li, M. Wu, X. Ji, X. Zeng and L. Mei, Dual-response oxygen-generating MnO2 nanoparticles with polydopamine modification for combined photothermal-photodynamic therapy, *Chem. Eng. J.*, 2020, **389**, 124494.
9 M. Luo, X. Zhu, H. Yang, L. Yan, R. Cai, Y. Zhao and W. Tan, Fabrication of AuPt heterostructured nanorings for enhanced synergistic radio-photothermal therapy, *Nano Today*, 2023, **51**, 101919.
10 L. Fu, Y. Wan, C. Qi, J. He, C. Li, C. Yang, H. Xu, J. Lin and P. Huang, Nanocatalytic theranostics with glutathione depletion and enhanced reactive oxygen species generation for efficient cancer therapy, *Adv. Mater.*, 2021, **33**(7), 2006892.
11 T. Chen, W. Zeng, Y. Liu, M. Yu, C. Huang, Z. Shi, C. Lin, J. Tang, L. Mei and M. Wu, Cu-doped polypyrrole with multi-catalytic activities for sono-enhanced nanocatalytic tumor therapy, *Small*, 2023, **19**(33), 202305389.
12 K. Hu, L. Xie, Y. Zhang, M. Hanyu, Z. Yang, K. Nagatsu, H. Suzuki, J. Ouyang, X. Ji, J. Wei, H. Xu, O. C. Farokhzad, S. Liang, L. Wang, W. Tao and M. Zhang, Marriage of black phosphorus and Cu2+ as effective photothermal agents for PET-guided combination cancer therapy, *Nat. Commun.*, 2020, **11**(1), 2778.
13 R. Cai, H. Xiang, D. Yang, K. Lin, Y. Wu, R. Zhou, Z. Gu, L. Yan, Y. Zhao and W. Tan, Plasmonic AuPt@CuS heterostructure with enhanced synergistic efficacy for radiophotothermal therapy, *J. Am. Chem. Soc.*, 2021, **143**(39), 16113–16127.
14 H. Su, Y. Wang, Y. Gu, L. Bowman, J. Zhao and M. Ding, Potential applications and human biosafety of nanomaterials used in nanomedicine, *J. Appl. Toxicol.*, 2018, **38**(1), 3–24.
15 S. Jin, S. Li, C. Wang, J. Liu, X. Yang, P. Wang, X. Zhang and X. Liang, Biosafe nanoscale pharmaceutical adjuvant materials, *J. Biomed. Nanotechnol.*, 2014, **10**(9), 2393–2419.

16 F. Zhao, Y. Guo, X. Zhou, W. Shi and G. Yu, Materials for solar-powered water evaporation, *Nat. Rev. Mater.*, 2020, **5**(5), 388–401.
17 Q. Meng, K. Cai, Y. Chen and L. Chen, Research progress on conducting polymer based supercapacitor electrode materials, *Nano Energy*, 2017, **36**, 268–285.
18 Y. Wang, W. Zeng, H. Liang, X. Wu, H. Li, T. Chen, M. Yang, X. Wang, W. Li, F. Zhang, Q. Li, F. Ye, J. Guan and L. Mei, Targeted wolfram-doped polypyrrole for photonic hyperthermia-synergized radiotherapy, *ACS Appl. Mater. Interfaces*, 2022, **14**(45), 50557–50568.
19 X. Wu, H. Liang, C. Li, D. Zhou and R. Liu, A hyperthermia-enhanced nanocatalyst based on asymmetric Au@polypyrrole for synergistic cancer Fenton/photothermal therapy, *RSC Adv.*, 2023, **13**(41), 29061–29069.
20 Y. Yang, F. Wang, J. Li, S. He, Y. Lyu, H. Yang, R. Cai and W. Tan, Self-powered biosensor based on DNA walkers for ultrasensitive microRNA detection, *Anal. Chem.*, 2023, **95**(40), 15042–15048.
21 F. Wang, H. Yang, J. Wu, Y. Lyu, K. Huang, R. Cai and W. Tan, An "On-Off" self-powered biosensor *via* GOD activated signal transduction for ultrasensitive detection of multiple biomarkers, *Chem. Eng. J.*, 2023, **468**, 143732.
22 F. Wang, R. Cai and W. Tan, Self-powered biosensor for a highly efficient and ultrasensitive dual-biomarker assay, *Anal. Chem.*, 2023, **95**(14), 6046–6052.
23 X. Wang, Y. Ma, X. Sheng, Y. Wang and H. Xu, Ultrathin polypyrrole nanosheets *via* space-confined synthesis for efficient photothermal therapy in the second near-infrared window, *Nano Lett.*, 2018, **18**(4), 2217–2225.
24 W. Zeng, X. Wu, T. Chen, S. Sun, Z. Shi, J. Liu, X. Ji, X. Zeng, J. Guan, L. Mei and M. Wu, Renal-clearable ultrasmall polypyrrole nanoparticles with size-regulated property for second near-infrared light-mediated photothermal therapy, *Adv. Funct. Mater.*, 2021, **31**(15), 2008362.
25 X. Wang, X. Ding, H. Zhao, J. Fu, Q. Xin and Y. Zhang, Pebax-based mixed matrix membranes containing hollow polypyrrole nanospheres with mesoporous shells for enhanced gas permeation performance, *J. Membr. Sci.*, 2020, **602**, 117968.
26 W. Zeng, M. Yu, T. Chen, Y. Liu, Y. Yi, C. Huang, J. Tang, H. Li, M. Ou, T. Wang, M. Wu and L. Mei, Polypyrrole nanoenzymes as tumor microenvironment modulators to reprogram macrophage and potentiate immunotherapy, *Adv. Sci.*, 2022, **9**(23), 2201703.
27 W. Feng, X. Han, R. Wang, X. Gao, P. Hu, W. Yue, Y. Chen and J. Shi, Nanocatalysts-augmented and photothermal-enhanced tumor-specific sequential nanocatalytic therapy in both NIR-I and NIR-II biowindows, *Adv. Mater.*, 2019, **31**(5), 1805919.
28 C. Huang, J. Tang, Y. Liu, T. Chen, J. Qi, S. Sun, H. Hao, W. Zeng, J. Zhao and M. Wu, Hyperthermia-triggered NO release based on Cu-doped polypyrrole for synergistic catalytic/gas cancer therapy, *Acta Biomater.*, 2023, **167**, 463–472.
29 B. Guo, J. Zhao, Z. Zhang, X. An, M. Huang and S. Wang, Intelligent nanoenzyme for T1-weighted MRI guided theranostic applications, *Chem. Eng. J.*, 2020, **391**, 123609.
30 K. Wen, L. Wu, X. Wu, Y. Lu, T. Duan, H. Ma, A. Peng, Q. Shi and H. Huang, Precisely tuning photothermal and photodynamic effects of polymeric nanoparticles by controlled copolymerization, *Angew. Chem., Int. Ed.*, 2020, **59**(31), 12756–12761.
31 Z. Yang, L. Zhang, J. Wei, R. Li, Q. Xu, H. Hu, Z. Xu, J. Ren and C. Wong, Tumor acidity-activatable photothermal/Fenton nanoagent for synergistic therapy, *J. Colloid Interface Sci.*, 2022, **612**, 355–366.
32 C. Sui, R. Tan, Z. Liu, X. Li and W. Xu, Smart chemical oxidative polymerization strategy to construct Au@PPy core-shell nanoparticles for cancer diagnosis and imaging-guided photothermal therapy, *Bioconjugate Chem.*, 2023, **34**(1), 257–268.
33 J. Song, X. Pan, J. Li, X. Hu and W. Yin, Characteristics of new oxygen-carrying plasma and its application prospects in the treatment of severe acute pancreatitis, *Pancreas*, 2023, **52**(1), E1–E6.
34 C. Xiao, J. Li, X. Wang, S. Li, C. Xu, Z. Zhang, A. Hua, Z. Ding, B. Zhang, X. Yang and Z. Li, Hydroxyethyl starch stabilized copper-diethyldithiocarbamate nanocrystals for cancer therapy, *J. Controlled Release*, 2023, **356**, 288–305.
35 H. Wang, H. Hu, H. Yang and Z. Li, Hydroxyethyl starch based smart nanomedicine, *RSC Adv.*, 2021, **11**(6), 3226–3240.
36 B. Kang, T. Opatz, K. Landfester and F. Wurm, Carbohydrate nanocarriers in biomedical applications: functionalization and construction, *Chem. Soc. Rev.*, 2015, **44**(22), 8301–8325.
37 R. Tan, Y. Wan and X. Yang, Hydroxyethyl starch and its derivatives as nanocarriers for delivery of diagnostic and therapeutic agents towards cancers, *Biomater. Transl.*, 2020, **1**(1), 46–57.
38 C. Wang, Q. Wang, H. Wang, Z. Li, J. Chen, Z. Zhang, H. Zeng, X. Yu, X. Yang, X. Yang and Z. Li, Hydroxyethyl starch-folic acid conjugates stabilized theranostic nanoparticles for cancer therapy, *J. Controlled Release*, 2023, **353**, 391–410.